



1 **Simulation of a lithosphere-atmosphere-ionosphere electromagnetic**
2 **coupling prior to the Wenchuan $M_S8.0$ earthquake**

3 Mei Li^{1,*}, Zhuangkai Wang², Chen Zhou², Handong Tan³, Meng Cao⁴

4
5 ¹Institute of Earthquake Forecasting, China Earthquake Administration, Beijing 100036, China

6 ²Department of Space Physics, School of Electronic Information, Wuhan University, Wuhan 430072, China

7 ³China University of Geosciences, Beijing 100083, China

8 ⁴Sichuan Hydropower Engineering Geophysical Exploration Co., Ltd, Chengdu 610072, China

9

10 *Correspondence to:* M. Li (mei_seis@163.com)

11

12 **Abstract** Continuously to a previous work on qualitatively investigating the probable electromagnetic
13 interacting process among lithosphere, atmosphere and ionosphere, this work aims to quantitatively
14 establish an electromagnetic coupling model among these three spheres prior to the Wenchuan
15 earthquake. Firstly, a underground finite length electrical dipole in a half-space model has been
16 employed to estimate the possible “energy source” for an observable 1.3 mV m^{-1} electrical field
17 registered at 1440 km Gaobeidian station during the Wenchuan event. The result shows that the
18 seismo-telluric current covers $\sim 10^5\text{--}10^6 \text{ kA}$ if the measuring frequency $f = 0.01\text{--}10 \text{ Hz}$ considered. The
19 central magnitude of the vertical electrical field caused by the current at 0.01 Hz on the Earth’s surface
20 can be up to kV m^{-1} . Then, this vertical field acts as an input into an electric field penetration model. It
21 is shown that this field attenuates quickly at the atmosphere and completely vanishes at the top
22 ionosphere and produces a 0.1 mV m^{-1} additional electrical field at the ionospheric bottom. Through
23 the TIE-GCM, this additional electrical field causes 0.01% ionospheric variations on electron density
24 and TEC near the Wenchuan epicenter, as well as near its magnetically conjugated point. Further, the
25 simulations have also been discussively performed on frequencies of 1 Hz and 10 Hz. The results
26 demonstrate that the variations of electron density present their maximum values at the height of $\sim 300\text{--}$
27 400 km and the varied percentages of ionospheric parameters have been beyond 10%, the same
28 magnitude as what has been registered during the Wenchuan shock.

29

30

31

32

33

34

35

36



37 **1. Introduction**

38 So far, short-term earthquake prediction is still one of the most challenging targets worldwide,
39 but the investigations on probable earthquake precursors in the fundamental geophysical framework
40 should be better than trying to guess the future (Eftaxias et al., 2003; Prescott, 2019; Hough, 2020;
41 Conti et al., 2021). An earthquake (EQ) is a systematical geodynamic process that develops gradually
42 as a strain accumulates slowly for several years, and culminates with a sudden rupture and
43 displacement of a fault in the rigid lithosphere (Bock, 1994). Exploring and understanding for possible
44 earthquake precursors, especially short-term ones, has been the most promising approach to short-term
45 earthquake prediction. Electromagnetic observing on possible information originated from seismic
46 activities is one of the most effective geophysical ways to snoop the last process of earthquake
47 evolutionary. But there is still a controversial understanding on the issue of mechanism on producing
48 and propagating of seismic signals from ground-based electromagnetic observation although pronounce
49 achievements have been gained on this problem. As Earth observation from satellite develops, more
50 and more reports have shown that the ionosphere, as a conductive part of the air, is unexpectedly
51 sensitive to seismic activities. Ionospheric measuring has gradually shown its potential application in
52 the field of earthquake monitoring and forecasting and emergency rescue due to its fast-speed, large-
53 scale, and high-resolution results, especially for areas with poor natural environments. In very recent
54 years, it has been testified that there is an energy transfer among lithosphere, atmosphere and
55 ionosphere at the last stages of earthquake preparation. Thus, a promising way to improve the
56 understanding on this complex geodynamic process is to integrate ground data with satellite Earth
57 Observation combined (De Santis et al., 2015).

58 Investigations on seismo-ionospheric influence or lithosphere-atmosphere-ionosphere coupling
59 (LAIC) mechanism has been primarily performed on the basis of two hypotheses: internal gravity
60 wave (IGW) or electric field.

61 Gokhberg et al. (2000) have found that the irregular ionospheric variations occurred several days
62 prior to strong earthquakes after an analysis of experimental data obtained at the last stage of
63 earthquake preparation. These ionospheric irregularities are attributed to the propagation of IGW
64 through the ionosphere and originated from the long wave earth oscillations, local green gas effect or
65 an unsteady injection of lithosphere. Thus, they have supposed that the generation of IGW (acoustic
66 gravity wave, AGW, after) should be considered as a mechanism of LAI coupling (Molchanov et al.,
67 2004; Meister et al., 2011). However, Sorokin & Hayakawa (2013, 2014) have presented that it is
68 difficult to interpret observing results of earthquake precursory information on the basis of IGW
69 propagation model due to its insufficient theoretical simulations and wave-like propagating features
70 (Conti et al., 2021). Therefore, it is easily to understand that investigations on LAI coupling transmit
71 from an acoustic-driven mechanism to an electromagnetic coupling due to its very low effectiveness
72 (Pulinets & Davidenko, 2014).

73 However, the electromagnetic “energy source” of the LAI coupling originated beneath the Earth
74 or in the atmosphere has still been under controversial. There are generally two different viewpoints:
75 electric sources beneath the Earth or ones on the ground. On one hand, scientists, who think that this
76 electromagnetic source is beneath the ground, have to confront with a problem, that is the producing
77 and propagating mechanism of electromagnetic emissions underground. Many laboratory and
78 wild-field rock fracturing experiments have broadly been conducted to understanding the producing
79 mechanism of electric and magnetic signals. Qian et al., (1996, 2003) have found that the large
80 magnetic pulses with shorter periods appeared at the last stage of the experiment. These relative high



81 frequency signals may be induced by instantaneous electric current of the accumulated charges during
82 the main cracking acceleration (Hao et al., 2003). While Freund et al. (Freund & Wengeler, 1982) have
83 proposed that seismo-telluric current may attribute to transmission of negative charge carriers and
84 positive holes from stressed rocks (Freund, 2002, 2009, 2010; Freund & Sornette, 2007; Scoville et al.,
85 2015). Up to now, several mechanisms, like electrokinetic and magnetohydrodynamic, piezomagnetism,
86 and microfracturing, have been proposed to explain the producing and propagating processes of electric
87 and magnetic emissions observed both during seismic activity and in the laboratory experiments but no
88 specified one has been well established (Conti et al., 2021; Heavlin et al., 2022). To construct
89 underground physical or mathematics models is always being an effective way to investigate this topic
90 (Huang, 2011; Huang & Lin, 2010; Ren et al., 2012).

91 On the other hand, investigators, who believe that the “electric energy” of the LAI coupling on the
92 ground, think that seismic activities can trigger off radon ionization, charged particulates injection and
93 changes in load resistance in global electric circuit, which further leads to zonal additional electrical
94 field near the ground (Pulinets & Ouzounov, 2010; Pulinets & Davidenko, 2014). While Sorokin &
95 Hayakawa (2013, 2014) have thought that injection of charged aerosols into the atmosphere acts as
96 electro-motive force to cause changes of conduction current in global electric circuit, which facilitates
97 the electrical field propagating vertically to the ionosphere. However, Pulinets & Davidenko (2014)
98 have reported that no scientific publications have demonstrated such injection of charged aerosols into
99 atmosphere before earthquakes, and the vertical external current flowing into the Global Electric
100 Circuit is absolutely impossible. Pulinets & Ouzounov (2010) have demonstrated that air ionization and
101 hydration processes induced by earthquakes in the vicinity of active tectonic faults change the global
102 electric circuit, which leads to a zonal additional electrical field near the Earth’s surface (Pulinets &
103 Davidenko, 2014). Kuo et al (2011, 2014) have investigated the LAI coupling on the basis of this
104 p-hole theory to consider stressed seismic fault as a dynamo to drive currents from stressed rocks to the
105 Earth’s surface. Zhou et al. (2017) have further developed an electrodynamic LAI coupling model
106 based on the DC electric field penetration and the results show that the LAIC electric field can
107 penetrate into a higher altitude in the ionosphere at a low latitude than at a high latitude. This
108 conclusion indicates that the additional electric field must be large enough during the LAI coupling if
109 expected observable plasma irregularity is obtained in the ionosphere. At the same time, an upper
110 atmosphere numerical model has been utilized to investigate the LAI coupling and the results have
111 displayed that seismogenerated zonal electric field can cause vertical plasma drift of F2 layer leading to
112 the disturbance of TEC (total electron content) (Namgaladze et al., 2012; Zolotov et al., 2012; Zolotov,
113 2015).

114 Additionally, thermal anomalies, such as ground surface latent flux and ongoing longwave
115 radiation (OLR), have also been considered as possible mechanism to drive LAI coupling but lacking
116 of a well-established model (Hayakawa & Pulinets, 2009, Pulinets et al., 2000; Liperovsky et al., 2008;
117 Freund, 2011). However, whatever the physical mechanism of the electromagnetic field generation is,
118 it seems that the electric sources or “energy sources” near the ground is undoubtedly a necessary part
119 during LAI coupling. Achieving a better understanding of a complex physics coupling of earthquakes
120 by the efforts of the involved scientific community worldwide will be dedicated to find a final answer
121 (De Santis et al., 2015; Conti et al. 2021).

122 At 14:28:01 CST (China Standard Time) on May 12, 2008, a large EQ with a magnitude of M_s 8.0
123 hit the Wenchuan area, Sichuan province, with an epicenter located at 103.4 °E and 31.0 °N and a depth
124 of 19 km. This event caused major extensive damage and 69,000 people lost their lives.



125 As a personal experience of tracing and recording measurement in Hebei observing network
126 during this large event (See the Supplement), Li et al. (2009) have firstly in Chinese and then in
127 English (Li et al., 2013) reported remarkable visible ULF ($f = 0.01\text{--}10$ Hz or its advantageous
128 frequency band $f = 0.1\text{--}10$ Hz) electromagnetic emissions of 1.3 mV m^{-1} electrical field recorded at the
129 1440 km Gaobeidian observing station during the Wenchuan EQ. Utilizing an ‘Earth-ionosphere’
130 physical model and a half-space model, Li et al. (2016) have modulated and interpreted the probability
131 of this abnormal phenomenon recorded at a far distance and inferred a possible seismo-elluric currents
132 at the depth of the Wenchuan hypocenter with and without ionospheric effect considered.

133 In this paper, on the basis of the work done by Li et al. (2016), this investigation mainly focuses
134 on the propagating process of the ground observable electrical field among the atmosphere and the
135 ionosphere, and the corresponding ionospheric influence caused by this field. So, in Section 2, in the
136 light of the observable electrical field registered during the Wenchuan EQ, we first utilize a half-space
137 model constructed by Li et al. (2016) to infer a probable underground seismo-elluric current, which
138 will act as the “energy source” driving the total LAI electromagnetic coupling. In Section 3, an electric
139 field penetration model developed by Zhou et al. (2017) will be employed to investigate the
140 propagating process of the electrical field induced by this current in the atmosphere and the ionosphere.
141 Additional electrical field at the bottom of the ionosphere will also calculated during this time. In
142 Section 4, ionospheric variations caused by this additional field will be evaluated using TIE-GCM
143 (Thermosphere-Ionosphere-Electrodynamics General Circulation Model) and compared with the
144 real-time ionospheric recordings during the Wenchuan event. Discussion and conclusions are in
145 Section 5 and Section 6, respectively.

146

147 **2. An estimation of the LAIC “energy source” associated with the Wenchuan EQ**

148 Li et al. (2009) have firstly presented that obvious ULF ($f = 0.01\text{--}10$ Hz) electromagnetic
149 emissions were recorded at 1440 km Gaobeidian station in Hebei observing network prior to the
150 Wenchuan $M_s 8.0$ EQ and the peak of the electrical signals reached 1.3 mV m^{-1} during the climax stage
151 of this anomaly. Then, Li et al. (2013) have established the relative locations of the Wenchuan epicenter
152 and the Hebei observing networks in Figure 1 to describe the electromagnetic anomaly recorded at the
153 remote observing stations. Further, Li et al. (2016) had employed two physical models of a half-space
154 model and an “Earth-ionosphere” model to gain the probability of this unprecedented anomaly
155 registered by such a remote station if the ionospheric influence considered. Their results have shown
156 that the ionosphere can promote the electromagnetic wave propagation, which is equivalent to an
157 effective improvement of the detectability of the system. The system could easily recorded signals
158 originated from the epicentral area of seismic activities even beyond its detectable range. At that time, a
159 surface coordinate system had been added to Figure 1 in Li et al. (2013) to form Figure 5 in Li et al.
160 (2016) to comply with the models and this figure has been also employed in this paper named Figure
161 1a.

162 Here, we use Figure 1a in this paper to exhibit the relative locations of the observing stations in
163 Hebei ULF electromagnetic observation network and the Wenchuan epicenter, as well as a surface
164 coordinate system. A half-space model utilized in Li et al. (2016) has also been employed here as
165 Figure 1b: An x-directed dipole with a length L and a current I is located in the bottom medium (Earth:
166 $z > 0$). Here the Earth is considered homogeneous, with the electrical properties: magnetic
167 permeability μ_1 , permittivity ϵ_1 , and conductivity σ_1 . The top medium (air: $z < 0$) is with electrical
168 properties μ_0 , $\epsilon_0 (= 8.854 \times 10^{-12}$ Farad m^{-1}) and $\sigma_0 (= 10^{-14}$ S m^{-1}).



169 The approach to investigate the electromagnetic fields emitted by a long dipole current source
 170 follows the magnetic vector potential formulation developed by Key (2009), who developed a
 171 generalized formulation for multiple layers below and above the transmitter. Exponential forms had
 172 been adopted for the recursions in isotropic media, with the z axis downward. Assuming a
 173 time-harmonic source with $e^{-i\omega t}$ time dependence, Maxwell's equations are

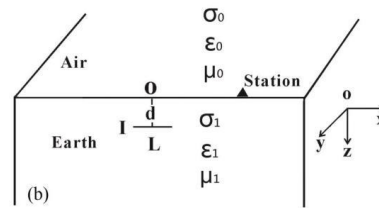
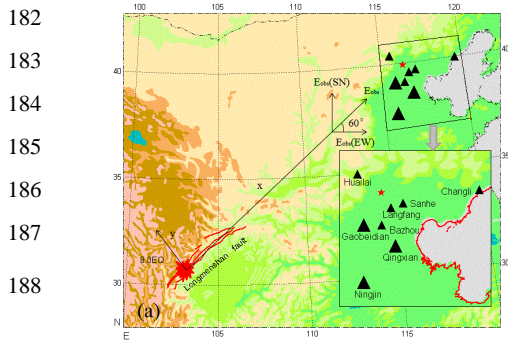
$$174 \quad \nabla \times \mathbf{E} = i\omega \mathbf{B}, \quad (1)$$

175 and

$$176 \quad \nabla \times \mathbf{B} = \mu\sigma \mathbf{E} + \mu \mathbf{J}_s. \quad (2)$$

177 where, magnetic permeability μ variations are negligible and angular frequency ω is low enough so
 178 that the displacement currents can be neglected. Expression $\mathbf{J}_s = \mathbf{I}\delta(\mathbf{r} - \mathbf{r}_0)$ is the imposed electric
 179 dipole source at position \mathbf{r}_0 with vector moment \mathbf{I} , and here is limited to an infinitesimal dipole with
 180 unit moment.

181



189

190 **Figure 1.** (a) Relative locations of the Wenchuan EQ epicenter and observation stations. Black solid triangles
 191 show observing stations in Hebei observing network and bigger ones indicate the stations recording abnormal
 192 information. The red star denotes Beijing (Li et al., 2013, Figure 1). A ground surface coordinate system has been
 193 formed by Li et al. (2016). (b) The half-space model: an x -directed dipole current source is placed in the bottom
 194 medium (Earth), and the dipole center coordinate is $(0, 0, d)$. Here, z is defined positive in the downward direction.

195

196 The total space is assumed to be non-magnetic and the magnetic permeability μ variations are
 197 negligible in the different layers, i.e. $\mu_1 = \mu_0 = 4\pi \times 10^{-7}$ Farad m^{-1} . On the same manner we
 198 have $\epsilon_1 = \epsilon_0 = 8.854 \times 10^{-12}$ Farad m^{-1} , i.e. ϵ_1 is not considered as zero during all calculations.
 199 The rupture length is set $L = 150$ km, within 30 s out of the total 90 s of the main Wenchuan rupture
 200 (Zhang et al., 2009) and the conductivity of the Earth is $\sigma_1 = 1.0 \times 10^{-3}$ S m^{-1} (Li et al., 2016)
 201 during the calculations. For an observed 1.3 mV m^{-1} electrical field at the Gaobeidian station, the
 202 expected seismo-elluric current falls in the range of $I = 1.5 \times 10^5 - 3.4 \times 10^6$ kA for the frequency range of
 203 $f = 0.01 - 10$ Hz. It can be seen that the current gradually increases as the observing frequency increases
 204 due to a dramatic attenuation of the electrical fields at higher frequency. This current induces
 205 electromagnetic emissions at the Earth's surface. Figure 2 displays two-dimensional distributions of
 206 three electrical components of E_x , E_y and E_z , respectively, produced at the Earth's surface by the
 207 seismo-elluric current $I = 1.5 \times 10^5$ kA when $f = 0.01$ Hz.

208



209

210

211

212

213

214

215

216

217

218

219

220

221

222

223

224

225

226 **Figure 2.** Two-dimensional distributions of electrical field components of (a) E_x , (b) E_y , and (c) E_z , respectively
227 induced by the Wenchuan seismo-current $I = 1.5 \times 10^5$ kA at $f = 0.01$ Hz after making a logarithm calculation at the
228 Earth's surface.

229

230 Figure 2 presents the 2-D power radiation patterns of three electrical components E_x , E_y , and E_z ,
231 respectively at the Earth's surface induced by the Wenchuan dipole source $I = 1.5 \times 10^5$ kA at $f = 0.01$
232 Hz within 1000 km from the epicenter. From Figure 2, we can see that the magnitude of the electrical
233 field intensity near the Wenchuan epicenter can be up to kV m^{-1} for each component, for instance, 10^2
234 kV m^{-1} for $f = 1$ Hz and 10^4 kV m^{-1} for $f = 10$ Hz. From this point, we also can infer that the maximum
235 electrical field at the ground for all frequency band of $f = 0.01\text{--}10$ Hz during the Wenchuan event can
236 beyond kV m^{-1} order. The maximum value central is 3.25 kV m^{-1} for the vertical field E_z at $f = 0.01$ Hz
237 near the center when the calculated electrical values have been examined, which will be as an input
238 into an electric field penetration model developed by Zhou et al. (2017) in the following part.

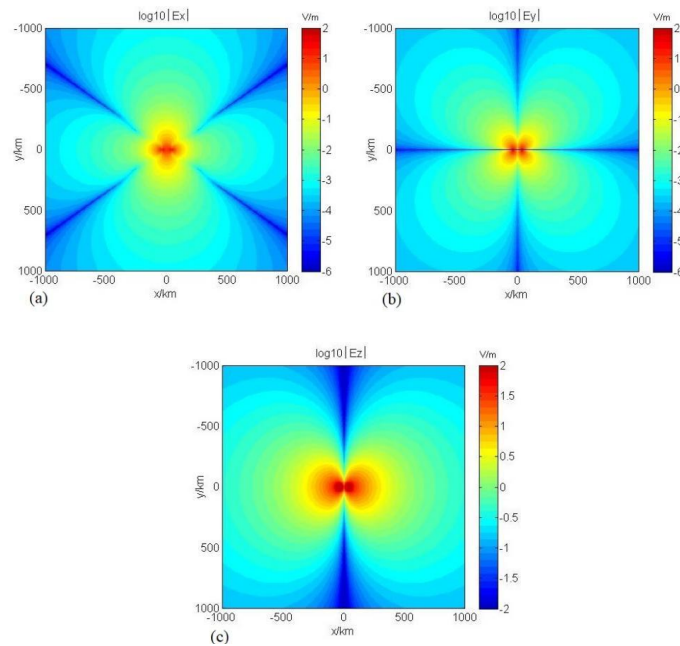
239

240 **3. Electrical coupling between the ground surface electromagnetic emissions and** 241 **ionosphere**

242 **3.1. Basic equations and boundary conditions**

243 The electric field penetration model developed by Zhou et al. (2017) has been briefly reviewed
244 first.

245 In the atmosphere, when the duration of a seismic event is equaling to or more than the
246 atmospheric electric field relaxation time τ_0 , the atmospheric condition can be transmitted from an
247 arbitrary initial state to a final steady state, which complies with the Ohm's law and the charge
248 conservation condition. Now, the electrostatic potential equation has been attained:





$$249 \quad -\nabla \cdot (\bar{\sigma} \cdot \nabla \Phi) = Q \quad (1)$$

250 where $\bar{\sigma}$ is the conductivity tensor.

251 In a Cartesian coordinate system, where, z -axis is vertically upward, x -axis is toward magnetic
 252 south, and y -axis is toward magnetic east,

253 Equation (Eq.) (1) can be written as

254

$$255 \quad \left(S^2 + \frac{\sigma_{\parallel}}{\sigma_P} C^2 \right) \frac{\partial^2 \Phi}{\partial x^2} + \frac{\partial^2 \Phi}{\partial y^2} + \left(C^2 + \frac{\sigma_{\parallel}}{\sigma_P} S^2 \right) \frac{\partial^2 \Phi}{\partial z^2} - 2 \left(1 - \frac{\sigma_{\parallel}}{\sigma_P} \right) CS \frac{\partial^2 \Phi}{\partial x \partial z} - \frac{CS}{\sigma_P} \left(\frac{\partial \sigma_P}{\partial z} - \frac{\partial \sigma_{\parallel}}{\partial z} \right) \frac{\partial \Phi}{\partial x} - \frac{C}{\sigma_P} \frac{\partial \sigma_H}{\partial z} \frac{\partial \Phi}{\partial y} +$$

$$256 \quad \frac{\partial(\sigma_P C^2 + \sigma_{\parallel} S^2)}{\sigma_P \partial z} \frac{\partial \Phi}{\partial z} = Q(x, y, z) \quad (2)$$

257

258 where σ_{\parallel} , σ_P and σ_H are the parallel, Pedersen and Hall conductivity, respectively. Magnetic field
 259 lines are in the x - z plane. I is the dip angle, $S = \sin I$, and $C = \cos I$. $Q(x, y, z)$ is the current source. In
 260 this LAIC model, we consider that the potential source is $j_z = \sigma_0 E_{z=0}$, and here $E_{z=0}$ is the vertical
 261 component of the electrical field induced at the Earth's surface by the Wenchuan seismo-elluric current
 262 I attained above and $Q(x, y, z) = 0$, which are treated as the lower boundary condition during the
 263 following calculations. However, a direct current is expected when this LAI coupling model developed
 264 by Zhou et al. (2017). Taking this limit under consideration, we have to assume that the ULF
 265 electromagnetic emissions appeared during the Wenchuan event meet the like-steady condition at the
 266 lower frequency band here. At the same time, Li et al. (2019) have qualitatively investigated the real
 267 time recordings from ground-based electromagnetic observation, geomagnetic observation and
 268 ionospheric observation occurred three days prior to the Wenchuan event. And the results show that
 269 their evolutionary processes in time reached the climax simultaneously within dozens of hours on 9
 270 May, which indicates the LAI coupling occurred.

271 For the upper boundary condition, z_{∞} has been set as the upper boundary of the ionosphere and
 272 no current flows out of this boundary. As we all know, variations of conductivity cover a large scale
 273 form the Earth's surface to ionosphere. Thus, the conductivity profile has been divided into three parts:

274 I neutral atmospheric region with $z < 50$ km, here the conductivity is considered to be isotropic,
 275 $\sigma_{\parallel}(0) = \sigma_P(0) = 1.0 \times 10^{-14} \text{ S m}^{-1}$ and $\sigma_{\parallel}(z) = \sigma_P(z) = \sigma(0) \exp\left(\frac{z}{6\text{km}}\right)$.

276 II atmosphere-ionosphere transition area with $50 \text{ km} < z < 90 \text{ km}$, wconsidering the continuity of
 277 the conductivity profile, we adopt the following formula: $\sigma_{\parallel}(z) = \sigma_1 \exp\left(\frac{z-50}{h_{\parallel}}\right)$, and $\sigma_P(z) =$
 278 $\sigma_1 \exp\left(\frac{z-50}{h_P}\right)$.

279 III ionosphere with $z > 90$ km, where the conductivity mainly depends on charged particles,
 280 cyclotron frequency of electron and ion, and their collision frequency, $\sigma_{\parallel} = \sum_a \frac{e^2 n_a}{m_a v_a}$, $\sigma_P =$
 281 $\frac{1}{B} \sum_a \frac{v_a \Omega_a}{v_a^2 + \Omega_a^2} e n_a$, and $\sigma_H = \frac{1}{B} \sum_a \frac{\Omega_a^2}{v_a^2 + \Omega_a^2} e n_a$, where a stands for the a species charged particles and
 282 n_a , v_a and Ω_a are the number density, collision frequency and cyclotron frequency of the particles.
 283 More details can be found in Zhou et al. (2017).

284

285 For high-latitude region, where the magnetic lines are vertical, the dip angle $I = 90^\circ$, $S = 1$ and C
 286 $= 0$. Eq. (2) can be simply written as:

287

$$288 \quad \sigma_{\parallel} \frac{\partial^2 \Phi}{\partial z^2} + \sigma_P \frac{\partial^2 \Phi}{\partial x^2} + \sigma_P \frac{\partial^2 \Phi}{\partial y^2} + \frac{\partial \sigma_{\parallel}}{\partial z} \frac{\partial \Phi}{\partial z} = 0 \quad (3)$$

289

290 With the lower-boundary and the upper-boundary conditions considered, the current distribution in
 291 the atmosphere will be attained by solving the electric potential Eq. (3), as well as in the ionosphere
 292 with the constrain of the conductivity defined above.



293 The simulation results gotten by Zhou et al. (2017) at high latitude have shown that the vertical
 294 current produced by the additional surface vertical electrical filed flows into the ionosphere without
 295 losing in the neutral atmosphere and then this current could induce abnormal ionospheric electrical
 296 field. This process at high latitude can also be suitable for low-mid latitude due to an exponential
 297 decrease of atmospheric conductivity, which is not dependent on a background magnetic line.

298 The current form the atmosphere has been considered as the source term and the electrical
 299 penetration model in the ionosphere can be solved referred to the propagation of thundercloud electric
 300 fields into the ionosphere. Under these conditions when the magnetic line is not vertical and the Earth's
 301 magnetic field is treated as a simple dipole field, Eq. (3) can be transformed into the form of the dipole
 302 coordinate system:

$$303 \quad \frac{\partial}{\partial t} \left(a \frac{\partial \Phi}{\partial t} \right) + \frac{\partial}{\partial \varphi} \left(b \frac{\partial \Phi}{\partial \varphi} \right) + \frac{\partial c}{\partial \varphi} \frac{\partial \Phi}{\partial t} - \frac{\partial c}{\partial t} \frac{\partial \Phi}{\partial \varphi} = - \frac{\partial}{\partial s} (h_{\varphi} h_t j_s) \quad (4)$$

$$304 \quad \text{where, } a = -\sigma_p \frac{h_{\varphi} h_s}{h_t}, \quad b = -\sigma_p \frac{h_t h_s}{h_{\varphi}}, \quad c = -\sigma_h h_s.$$

305 Considering the conjugated effect (the potentials of ionospheric south and north ends of a
 306 magnetic line equals each other due to a high ionospheric conductivity), Eq. (4) can be integrated along
 307 the magnetic field lines connecting the lower boundaries of the opposite hemispheres:

$$308 \quad A \frac{\partial^2 \Phi}{\partial z^2} + B \frac{\partial^2 \Phi}{\partial \varphi^2} + D \frac{\partial \Phi}{\partial t} + E \frac{\partial \Phi}{\partial \varphi} = F \quad (5)$$

309 where A, B, C, D, E and F are parameters concerned with $a, b, c, h_{\varphi}, h_t, h_s$ in equation (4), S_1 and
 310 S_2 are the lower and upper boundaries of the northern hemisphere, S_3 and S_4 of the southern
 311 hemisphere, respectively. The range of the conductive ionosphere has been set to 90–500 km. More
 312 details can be seen in Zhou et al. (2017).

313 Eq. (5) is the ionospheric potential equation. Unlike Eq. (3), Eq. (5) is a two-dimensional
 314 equation but with a nonhomogeneous term as the electrical field source propagating along s direction:
 315 j_{s1} and j_{s2} in lower and upper northern ionospheric boundaries. When the region taken part in
 316 calculation is far away from the pole and the magnetic equator, the solution area is $(t_{\min} \times t_{\max}) \times$
 317 $(\varphi_{\min} \times \varphi_{\max})$, where $t_{\max} = t_0 + 0.1$ and $t_{\min} = t_0 - 0.1$ are the magnetic field lines close to and
 318 far away from respectively the magnetic equator, and $\varphi_{\min} = \varphi_0 - \frac{10}{360}\pi$ and $\varphi_{\max} = \varphi_0 + \frac{10}{360}\pi$
 319 are the left and right boundaries of the magnetic longitude. If this boundary is far away from the
 320 areawhere the current flows, Dirichlet conditions are well met and the boundary potential can be
 321 considered to 0:

$$322 \quad \Phi(t_{\min, \max}, \varphi) = 0 \quad \text{and} \quad \Phi(t, \varphi_{\min, \max}) = 0 \quad (6)$$

323 Under these boundary conditions, the potential of the ionosphere in Eq. (5) is a 2D elliptic partial
 324 differential equation and can be solved using a relaxation iterative method. Combined with Eq. (4) and
 325 the solution of Eq. (5), the distribution of electric field in the ionosphere will be attained.

327 3.2. Propagation of additional current in atmosphere and ionosphere

328 The current density on the ground can be attained $j_z = \sigma_0 E_{z=0}$ when the conductivity
 329 $\sigma_0 = 10^{-14} \text{ S m}^{-1}$, where $E_{z=0}$ is the calculated vertical electrical field by the Wenchuan source $I =$
 330 $1.5 \times 10^8 \text{ A}$ at $f = 0.01 \text{ Hz}$ at the Earth surface and its radiation pattern could be refer to Figure 2c in
 331 Section 2. Thus, we can attain that the maximum value of the current density near the Wenchuan
 332 source at the Earth's surface $j_{\max(z=0)}$ is of $10^{-11} \text{ A m}^{-2}$. This current propagates upward continuously
 333 among the atmosphere and the ionosphere. Equations established and related boundary conditions in
 334 Section 3.1 have been utilized to simulate this process.



335 Figure 3 presents two-dimensional distributions of calculated electrical fields of (a) north
336 component E_x , (b) east component E_y , and (c) vertical component E_z , respectively in the magnetic x-y
337 plane at the ionospheric bottom with an altitude $z = 90$ km. It is apparently shown that the induced
338 electrical field with kV m^{-1} at the ground surface (See Figure 2) has been subjected to a severe
339 attenuation in the atmosphere to 0.1mV m^{-1} magnitude at the ionospheric bottom. Zhou et al. (2017)
340 have demonstrated that, compared with high latitude region, in the mid-low latitudinal regions, the
341 intensity of the total horizontal electric field increases with the latitude and the vertical electric field is
342 more evident at low latitudes

343 On one hand, this current propagates continuously with a rapid attenuation in the well-conductive
344 ionosphere. Figure 4 exhibits the vertical electrical field distribution of this current flow in x-z plane
345 with an increasing altitude under the constraint of conductivity defined above. As presented in Figure 4,
346 the vertical current splits from its source and transmits in the ionosphere continuously with a rapid
347 attenuation, especially for the height beyond 150 km and eventually vanishes at the top of the
348 ionosphere with $z = 500$ km. The penetration height of additional electric field in the ionosphere is
349 higher at high latitudes than that at low latitudes (Zhou et al., 2017). On the other hand, the additional
350 electrical current from the atmosphere modifies the ionospheric parameters either by heating the
351 ionosphere or by the plasma drifting in the electrical field of this current (Ruzhin et al., 2014). Thus,
352 the additional potential determined by this current will be considered as an input in the following part.

353
354

355

356

357

358

359

360

361

362

363

364

365

366

367

368

369

370

371

372

373

374

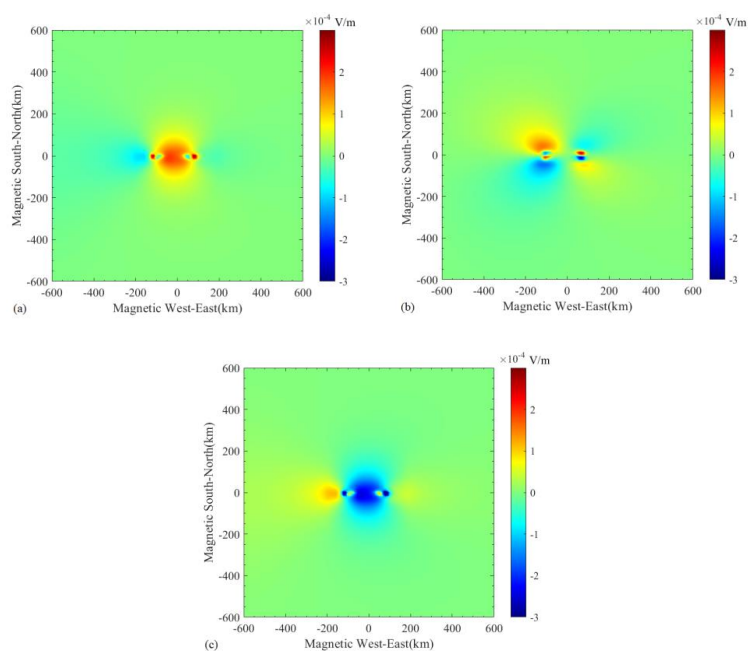
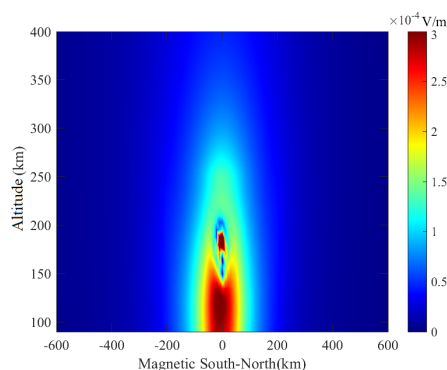


Figure 3. Two-dimensional distributions of the calculated electric field components at the ionospheric bottom (altitude 90 km) when the surface vertical current source of Figure 2c as an input into the atmosphere-ionosphere coupling model. This current source is the induction at the Earth surface from the Wenchuan finite length dipole at the operating frequency $f = 0.01$ Hz. (a) Horizontal north field E_x ; (b) Horizontal east field E_y ; (c) Vertical field E_z .



375
376
377
378
379
380
381
382
383
384
385
386



387
388
389

Figure 4. Distribution of the additional vertical electrical field caused by the Wenchuan source at the frequency $f = 0.01$ Hz at x-z plane in the ionosphere.

390

4. Ionospheric variations caused by the additional potential

391
392
393
394
395
396
397
398
399
400
401
402
403

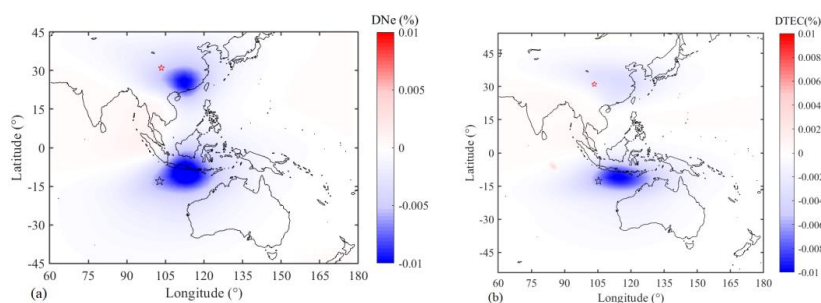
Here, the TIE-GCM (Thermosphere-Ionosphere-Electrodynamics General Circulation Model) has been employed to attain ionospheric modifications caused by the Wenchuan source at the frequency $f = 0.01$ Hz. The TIE-GCM is a self-consistent physical model developed by National Center for Atmospheric Research (NCAR) and it is a comprehensive thermosphere and ionosphere coupling system to solve the three-dimensional momentum, energy and continuity equations for neutral and ion species using finite difference method. With polar particle deposition, high latitude electrical field and tidal effect from lower atmosphere considered, the TIE-GCM can calculates global distributions of the neutral gas temperature and winds, the height of the constant pressure surface and the number densities of the major constituents within the altitude 90–700 km when several parameters, such as F10.7 daily index, Kp index, etc. act as input (Roble et al., 1988; Richmond et al., 1992; Rougier et al., 2007). The additional potential induced by the Wenchuan source at the bottom of the ionosphere also as an input into this dynamic model after some modifications on its original codes.

404
405
406
407
408
409
410
411
412
413
414
415
416
417
418

Figure 5 demonstrates ionospheric influence with percentages of the additional potential on the electron density (Ne) at an altitude ~400 km (Figure 5a) and the total electron content (TEC) (Figure 5b). From Figure 5, it is clear that the additional potential from the Wenchuan source can causes ionospheric variations on both parameters in the Wenchuan epicentral area, as well as in its magnetically conjugated area, which is highly coincident with what have been described by most authors (Zhao et al., 2010; Liu et al., 2009; Pulinets et al., 2009; Yan et al., 2012; and references therein) in light of real-time ionosphere measurement. But the variation in this time is with a little magnitude of ~0.01%. Many documents have presented positive and negative variations on these both parameters at the opposite hemispheres prior to the Wenchuan EQ (Zhao et al., 2008; Yu et al., 2009; Liu et al., 2015; Akhoondzadeh et al., 2010; Pulinets & Ouzounov, 2011; and references therein). He et al. (2011) have reported a 30% increase of electron density during the Wenchuan event. Zeng et al. (2009) have presented more than 20% variations on electron density, electron temperature and O^+ density. It also has been reported 20%–60% negative and positive fluctuations on TEC prior to this event (Yan et al., 2012; Yu et al., 2009). Comparatively, the simulation results in this time are less far from real-time recordings by different sensors.



419
420
421
422
423
424
425
426
427
428
429
430



431 **Figure 5.** Ionospheric influence of the Wenchuan source at $f = 0.01$ Hz on (a) electron density Ne and (b) the total
432 electron content TEC. The Wenchuan epicenter and its magnetically conjugated point have been labeled by a red
433 star and a black star, respectively in each panel.
434

435 5. Discussion

436 The fact that abundant electromagnetic emissions on ULF–ELF electrical field (Li et al., 2009,
437 2013; Gao et al., 2010; An et al., 2013; Jin et al., 2020), as well as ULF geomagnetic anomaly (Hu et
438 al., 2009; Wang et al., 2009; Hayakawa et al., 2015; Li et al., 2015; Cheng et al., 2010; Li et al., 2019),
439 before the 12 May 2008 Wenchuan $M_s 8.0$ earthquake have been gradually reported. At the same time,
440 ionospheric variations registered by different equipment of ground-based ionosonde data (Zhao et al.,
441 2008; Sun et al., 2011; Maurya et al., 2013; and references therein), DEMETER satellite data (Zhang
442 et al., 2009; Onishi et al., 2011; Liu et al., 2015; Walker et al., 2013; and references therein),
443 ground-based GPS satellite data (Zhao et al., 2010; Liu et al., 2009; Pulinets et al., 2009; Zhu et al.,
444 2009; and references therein), radio occultation data from six microsattellites of
445 FORMOSAT3/COSMIC (F3/C) data (Liu et al., 2009; Ma et al., 2014; Hsiao et al., 2010), and
446 CHAMP (challenging minisatellite payload) satellite data (Ryu et al., 2014) have also been confirmed
447 as an increasing number of literatures published. These anomalies present different time scales and
448 varied magnitudes but take on a common climax on May 9, 2008, three days prior to the Wenchuan
449 main event, which undoubtedly raises an upsurge on theoretical or speculative interpreting them and
450 investigating a probable LAI coupling concerned with all aspects on its mechanism.

451 Li et al. (2019) have qualitatively analyzed temporal variation orders of ground-based ultra-low
452 frequency (ULF) electrical field, geomagnetic field and ionospheric parameters occurred on May 9
453 2008. They results indicate an LAIE coupling process: the electromagnetic energy propagates from the
454 epicentral area to the Earth’s surface, via the atmosphere and ionosphere, finally to its magnetically
455 conjugated area in the opposite hemisphere, causing ground-based, atmospheric and ionospheric
456 electromagnetic disturbances, in that order. In this research, theoretical simulations on this LAI
457 electromagnetic coupling process have been performed on the basis of an observable 1.3 mV m^{-1} ULF
458 ($f = 0.01\text{--}10$ Hz) electrical field registered at 1440 km Gaobeidian observing station in Hebei Province.
459 An infinite length electrical dipole in half-space model has been utilized beneath the Earth to estimate
460 the “energy source” of this LAI coupling and the calculated seismo-telluric current I lies in the range of
461 $1.5 \times 10^5\text{--}3.4 \times 10^6$ kA corresponding to the frequency range of $f = 0.01\text{--}10$ Hz. Bortnik et al. (2010) have
462 employed an electrical dipole collocated with the 31 October 2007 “Alum Rock” $M_w = 5.6$ earthquake



463 hypocenter to interpret an observable 30 nT pulse at 1 Hz and $D = 2$ km and their results present an
464 estimated seismo-telluric current ~ 10 – 100 kA. Comparatively, the result attained in this time is
465 probably in a reasonable range (Li et al., 2016).

466 In the atmosphere, an electrical field penetration model developed by Zhou et al. (2017) has
467 been used to simulate the propagating properties of the surface current from the Wenchuan source.
468 Corresponding to the direct current in this model, the vertical electrical field E_z produced by the
469 seismo-telluric current $I = 1.5 \times 10^5$ kA at $f = 0.01$ Hz has acted as the primary input into this model.
470 The central magnitude of this input electrical field on the ground surface can be up to kV m^{-1} and this
471 field attenuates to the order of 0.1 mV m^{-1} at the bottom ($z = 90$ km) of the ionosphere, which merely
472 leads to $\sim 0.01\%$ variations on electron density at the altitude 400 km and TEC in the ionosphere, an
473 incomparable value with real-time measured. Concerned with the electrical penetration model, Zhou et
474 al. (2017) have proposed that 1000 V m^{-1} vertical electrical field on the ground can generate $1.1 \times 10^{-6} \text{ V}$
475 m^{-1} electrical field at the ionospheric bottom at the magnetic latitude of 30°N , which is too smaller than
476 background ionosphere electrical field of 1 – 3 mV m^{-1} to generate ionospheric fluctuations by
477 electrodynamic processes. Therefore, a dramatic increase in atmospheric conductivity by neutral
478 atmosphere ionizing is suggested by Zhou et al. (2017).

479 Kuo et al. (2014) have presented a 20% ionospheric variation induced by 5 mV m^{-1} electrical
480 field corresponding to 100 nA m^{-2} current density at the ground surface. To get an obvious ionospheric
481 variations, by an LAI coupling model, Kim & Hegai (1999) and Pulinetz et al. (2000) proposed that
482 obvious vertical electric fields at the Earth's surface could transmit into the ionosphere via the
483 atmosphere and modify dynamic and electronic properties of the ionosphere prior to the earthquake
484 Their results have presented that a $\sim 1 \text{ kV m}^{-1}$ vertical electric field at the Earth's surface can be
485 expected to produce a $\sim 1 \text{ mV m}^{-1}$ horizontal electric field at the ionospheric heights to give rise to
486 obvious ionospheric variations.

487 Sorokin & Hayakawa (2013, 2014) have presented that the injection of charged aerosols into
488 the atmosphere acts as an additional EMF (electro-motive force) in the global circuit. Under this
489 condition, the total electric current can be written as $\mathbf{j} = \sigma \mathbf{E} + \mathbf{j}_e$, here \mathbf{j}_e is EMF external current and $\sigma \mathbf{E}$
490 is conductive current. The additional electrical field can be up to 10 mV m^{-1} leading to ionospheric
491 variations when the EMF external current acts as a compensate term during the conductive current
492 propagating up to the ionosphere. On the basis of model, Yang et al. (2014) have performed a
493 numerical simulation on seismic-related DC electric field during atmosphere-ionosphere coupling.
494 Their results have presented that the horizontal scale of electric field in the ionosphere is larger than
495 that of the external current in the atmosphere and this current can induce much larger electric field at
496 night than during the day.

497 As a discussion, we have also performed all corresponding calculations on other observing
498 frequencies at $f = 1$ Hz and $f = 10$ Hz, respectively, like done on $f = 0.01$ Hz. The calculated
499 magnitudes of ground-surface vertical electrical fields near the central points for these two frequencies
500 can be up to 10^2 kV m^{-1} and 10^4 kV m^{-1} , corresponding to respective ionospheric-bottom electrical
501 fields of $\sim 200 \text{ mV m}^{-1}$ and $\sim 1000 \text{ mV m}^{-1}$. Figure 6 shows differences of electron density (DNe) for
502 different layers defined in TIE-GCM model of 10 (~ 100 km in altitude), 30 (~ 200 km), 35 (~ 250 km),
503 40 (~ 300 km), 50 (~ 400 km) and 55 (~ 450 km) due to an input electrical potential determined by the
504 Wenchuan source at the frequency $f = 1$ Hz. As shown in Figure 6, the patterns and the magnitudes of
505 the DNe during this period are variable in different altitudes near the epicenter and its magnetically
506 conjugated area. It is shown clearly that the magnitude of positive variations increases as the altitude



507 increases below ~300 km and can reach 5% at 200–300 km, while the maximum varied magnitude can
508 be up to 10% but with negative anomaly at ~400 km, which is highly coincident with the work done by
509 He & Heki (2016, 2018). They have investigated the variations of the total electron content (TEC)
510 before two mid-latitude EQs of the 2010 Maule M_w 8.8 EQ and the 2015 Illapel M_w 8.3 EQ in Chile and
511 the results have demonstrated that the ionospheric anomalies have displayed both positive and negative
512 regions, with different altitudes of ~200 km and ~400 km, respectively, distributing roughly along the
513 geomagnetic fields.

514

515

516

517

518

519

520

521

522

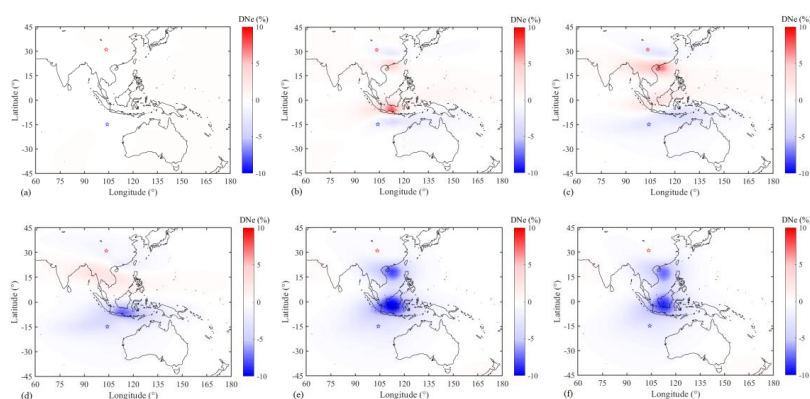
523

524

525

526

527



528

529

530

531

532

533

534

535

536

537

538

539

540

541

542

543

544

545

546

547

548

549

550

Figure 6. Ionospheric influence of the Wenchuan source at $f = 1$ Hz on electron density Ne at different layers defined by the TIE-GCM model. The Wenchuan epicenter and its magnetically conjugated point have been labeled by a red star and a blue star, respectively in each panel. (a) layer 10 (~100 km in altitude), (b) 30 (~200 km), (c) 35 (~250 km), (d) 40 (~300 km), (e) 50 (~400 km) and (f) 55 (~450 km).

Figure 7 exhibits ionospheric influence with percentages of the additional potential on the electron density (Ne) at an altitude ~400 km (Figure 5a) and the total electron content (TEC) (Figure 5b). From Figure 7, it is clear that the additional potential from the Wenchuan source can cause negative variations on both parameters in the Wenchuan epicentral area, as well as in its magnetically conjugated area. The varied percentage could be up to 15%, and this value is also consistent with the real-time measured magnitude.

540

541

542

543

544

545

546

547

548

549

550

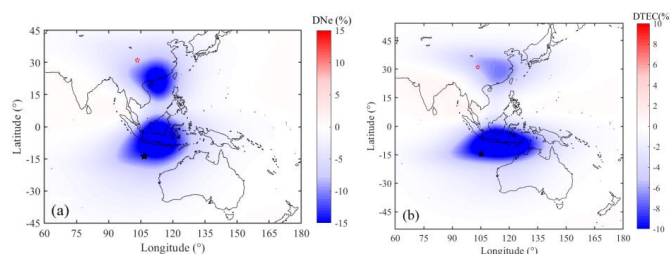


Figure 7. Ionospheric influence of the Wenchuan source at $f = 10$ Hz on (a) electron density Ne at the high altitude 400 km and (b) the total electron content TEC. The Wenchuan epicenter and its magnetically conjugated point



551 have been labeled by a red star and a blue star, respectively in each panel.

552

553 Apparently, variations of ionospheric parameters seem to be approximately proportional to the
554 magnitude of the additional potential input. The varied magnitude on both parameters of electron
555 density and the total electron content is covering 0.01–15% corresponding to the observing frequency
556 band of $f = 0.01\text{--}10$ Hz during the Wenchuan event. While this potential magnitude has been
557 determined by the frequency of the signals observed during the earthquakes. Concerned with
558 electromagnetic signals originated from seismic activities, on one hand, ULF signals can propagate to
559 the ground surface due to their lower attenuation beneath the Earth. Li et al., (2013) have reported
560 $\sim 0.1\text{--}0.3$ s electrical signals recorded during the climax stage of the anomaly before the Wenchuan
561 main event. On the other hand, most experimental and real-time recordings have demonstrated that
562 signals with relatively higher frequencies appear during the main rupture of strong seismic events,
563 where the main rupture refers to a process of micro-cracks quickly developing into macro-rupture for
564 pressed fault (Li et al., 2013; Qian et al., 1996, 2003; Hao et al., 2003). Please note, this rupture
565 probably happens from the hypocentral depth till to the near Earth's surface during this period instead
566 of only focusing on the small area around the hypocenter of an impending earthquake. Therefore, even
567 signals with higher frequency than the ULF band can also easily propagate out of the Earth. Li et al.
568 (2013) have also noticed that the climax occurred on May 9, 2008, three days prior to the Wenchuan
569 main event, which indicates that an integrated effect of the electrical signals with different frequencies
570 acts as persisting current equivalent to a direct current to cause a LAI coupling.

571 A direct current electrical penetration model has been utilized here to simulate and interpret the
572 processing of the electrical current propagating in the atmosphere and ionosphere and simultaneously
573 causing ionospheric influence. It is noticed from the simulation results that the patterns of the
574 ionospheric variations are similar to what have been depicted in different literatures (Zhao et al., 2010;
575 Pulinets et al., 2010; Ryu et al., 2014; *and references therein*): the anomalies appear in bothside
576 hemispheres with a shift to the equator. Also, previous researches have shown that the location of
577 ionospheric effect is not coincident right with the vertical projection of the epicenter of the appending
578 earthquake but shifts equatorward at high and middle latitudes. Li et al., (2023) have reported statistical
579 seismo-ionospheric influence performed by electron density measured by the CSES (China Seismo-
580 Electromagnetic Satellite) for more than three years shifts 500–700 km away instead of right above the
581 epicenters for strong seismic activities in mid-low latitudes. Liu et al. (2009) have presented that the
582 eastward plasma $E \times B$ drift causes the GPS TEC enhancement slightly shifting to the east side of the
583 Wenchuan epicenter, although the generated mechanism is not understood. The enhanced GPS TEC
584 appeared in the southern China with a rounded shape, which is usually under control of the northern
585 equatorial ionization anomaly (EIA). So, bothside ionospheric anomalies generally shift toward the
586 equatorial area due to double crests of the EIA (Pulinets & Boyarchuk, 2004; Liu et al., 2009; Zhao et
587 al, 2008).

588 The ionospheric effect over the seismic activity areas in one hemisphere, as well as over their
589 magnetical conjugation areas in the opposite hemisphere could be depicted along the geomagnetic field
590 lines (Pulinets & Boyarchuk 2004). It is possible the space distribution of the TEC influence has been
591 determined by the joint effect of the two factors: the heating on the ionospheric properties by electric
592 current and the plasma drift in the electric field caused also by this current. The resulting $E \times B$ drift
593 should lead to a redistribution of plasmatic parameters over the earthquake preparation zone, as well as
594 over its magnetically conjugated area. The ionospheric anomalies in both sides of the sphere locate on



595 different sides of the magnetic meridian, which passes through the earthquake epicenter and its
596 magnetic conjugate point (Ruzhin, et al., 2014). However, the central points of the ionospheric
597 abnormalities on both hemispheres in this time seem to locate the same side of the magnetic meridian
598 (see Figures 5–7). Also, noticed that, the spatial distribution and patterns of ionospheric variations
599 could change with the shape and direction of the underground source during the calculation. However,
600 we cannot determine the right shape of the real source causing by an earthquake. Another point is, the
601 atmosphere, as a common part of the half-space model and the electrical penetration model utilized in
602 this time, is of different properties: homogeneous medium with a specified conductivity in the first
603 model and inhomogeneous medium with various parallel conductivity σ_{\parallel} , Pedersen conductivity σ_P
604 and Hall conductivity σ_H along the altitude in the second one, which could affect the final results. A
605 comprehensive model with more precise lithospheric and atmospheric conductivity information will be
606 expected to gain more reasonable results in the future.

608 6. Conclusions

609 This investigation aims to tentatively establish an LAI electromagnetic coupling process model in
610 the light of several physical models and real-time recordings of different spheres before the Wenchuan
611 $M_S 8.0$ earthquake. A finite length electrical dipole in a half space model has been firstly employed to
612 estimate the possible magnitude of the “energy source” for an observable 1.3 mV m^{-1} electrical field at
613 1440 km Gaobeidian station. The results show that the expected seismo-telluric current falls in the
614 range of $I = 1.5 \times 10^5 \text{--} 3.4 \times 10^6 \text{ kA}$ if the observing ULF band of $f = 0.01\text{--}10 \text{ Hz}$ has been considered.
615 The electrical fields induced by this seismo-telluric current propagate from the Wenhuan hypocentral
616 area to the ground and the magnitudes of their vertical components are beyond kV m^{-1} at the Earth’s
617 surface, which will act as the input of the “energy source” arousing a coupling between the atmosphere
618 and the ionosphere.

619 Then, the electric field penetration model developed by Zhou et al., (2017) has been utilized here
620 to simulate the propagating process of the electrical field from the ground on one hand, and get the
621 additional electrical field at the bottom of the ionosphere at 90 km, on the other hand. It has been
622 testified that the magnitude of the additional electrical field at the bottom of the ionosphere ranges from
623 0.1 mV m^{-1} to 1000 mV m^{-1} if the observing frequency considered and then this field is subjected to a
624 severe decay in the well conductive ionosphere.

625 Finally, the magnitude of ionospheric variations induced by the additional field at the ionospheric
626 bottom has been simulated by the TIE-GCM and the expected results can be up to 15% if combined
627 effect of all recorded signals considered, which basically keeps the same magnitude as real-time
628 ionospheric measurements. However, much work, such as, selections of parameters, construction of a
629 comprehensive theoretical physical model, and so on, will be improved in the near future.

630

631

632 Competing interests

633 The contact author has declared that none of the authors has any competing interests.

634

635

636 Acknowledgments

637 This work was supported by the National Natural Science Foundation of China (NSFC) under Grant No. 41774084.

638 National Center for Atmospheric Research (NCAR) is supported by the National Science Foundation. The



639 TIEGCM model can be downloaded at <http://www.hao.ucar.edu/modeling/tgcm/download.php>.

640

641 **Data Availability Statement**

642 All data and code utilized in this manuscript can be downloaded at <https://www.alipan.com/s/PRsZpAyoh3p>.

643

644

645 **References**

646 Akhoondzadeh, M., Parrot, M., & Saradjian, M. R. (2010). Electron and ion density variations before strong
647 earthquakes ($M > 6.0$) using DEMETER and GPS data. *Nat. Hazards Earth Syst. Sci.*, *10*(1), 7–18.

648 <https://doi.org/10.5194/nhess-10-7-2010>

649 An, Z., Du, X., Tan, D., Fan, Y., Liu, J., & Cui, T. (2013). Study on the geo-electrical field variation of Sichuan
650 Lushan M_s 7.0 and Wenchuan M_s 8.0 earthquake. *Chinese J. Geophys.*, *56*, 3868–3876 (in Chinese with
651 English abstract).

652 Bock, Y. (1994). Crustal deformation and earthquakes. *Geotimes*, *39*(6), 16–18.

653 Bortnik, J., Bleier, T. E., Dunson, C., & Freund, F. (2010). Estimating the seismotelluric current required for
654 observable electromagnetic ground signals, *Ann. Geophys.*, *28*, 1615–1624.

655 Cheng, F., Ren, Y., & Wu, X. (2010). Analyzing the anomalies of geo-electrical and geo-magnetic observation
656 data in Sichuan Province before the 2008 Wenchuan M 8.0 Earthquake. *Earthq. Res. Sichuan*, *135*, 2–9
657 (in Chinese with English abstract).

658 Conti, L., Picozza, P., & Sotgiu, A. (2021). A critical review of ground based observations of earthquake
659 precursors. *Front. Earth Sci.*, *9*, 676–766. <https://doi.org/10.3389/feart.2021.676766>

660 De Santis, A., Franceschi, G. D., Spogli, L., Perrone, L., Alfonsi, L., Qamili, E., Cianchini, G., Giovambattista, R.
661 D., Salvi, S., Filippi, E., Pavon-Carrasco, F.J., Monna, S., Piscini, A., Battiston, R., Vitale, V., Picozza, P. G.,
662 Conti, L., Parrot, M., Pincon, J. L., Balasis, G., Tavani, M., Argan, A., Piano, G., Rainone, M. L., Liu, W., &
663 Tao, D. (2015). Geospace perturbations induced by the Earth: The state of the art and future trends. *Physics and
664 Chemistry of the Earth*, *85–86*, 17–33. <https://doi.org/10.1016/j.pce.2015.05.004>

665 Eftaxias, K., Kapiris, P., Polygiannakis, J., Peratzakis, A., Kopanas, J., Antonopoulos, G., & Rigas, D. (2003).
666 Experience of short term earthquake precursors with VLF-VHF electromagnetic emissions. *Nat. Hazards Earth
667 Syst. Sci.*, *3*, 217–228. <https://doi.org/10.5194/nhess-3-217-2003>, 2003

668 Freund, F., & Wengeler, H. (1982). The infrared spectrum of OH-compensated defect sites in C-doped MgO and
669 CaO single crystals. *J. Phys. Chem. Solids*, *43*, 129–145. [https://doi.org/10.1016/0038-1098\(82\)90739-6](https://doi.org/10.1016/0038-1098(82)90739-6)

670 Freund, F. (2002). Charge generation and propagation in igneous rocks. *J. Geodynamics*, *33*, 543–
671 570. [https://doi.org/10.1016/s0264-3707\(02\)00015-7](https://doi.org/10.1016/s0264-3707(02)00015-7)

672 Freund, F. (2009). Stress-activated positive hole charge carriers in rocks and the generation of pre-earthquake
673 signals, in: *Electromagnetic Phenomena Associated with Earthquakes*, edited by: Hayakawa, M., *Transworld
674 Research Network, Trivandrum, India*, *3*, 41–96.

675 Freund, F. (2010). Toward a unified solid state theory for pre-earthquake signals. *Acta Geophys.*, *58*, 719–766.
676 <https://doi.org/10.2478/s11600-009-0066-x>

677 Freund, F., & Sornette, D. (2007). Electro-magnetic earthquake bursts and critical rupture of peroxy bond
678 networks in rocks. *Tectonophysics*, *431*, 33–47. <https://doi.org/10.1016/j.tecto.2006.05.032>

679 Freund, F. (2011). Pre-earthquake signals: Underlying physical processes. *J. Asian Earth Sci.*, *41*(4–5), 383–400.
680 <https://doi.org/10.1016/j.jseas.2010.03.009>

681 Gao, S., Tang, J., Du, X., Liu, X., Su, Y., Chen, Y., Di, G., Mei, D., Zhan, Y., & Wang, L. (2010). The change
682 characteristics of electromagnetic field before to after Wenchuan M_s 8.0 earthquake. *Chinese J. Geophys.*, *53*,



- 683 512–525 (in Chinese with English abstract).
- 684 Gokhberg, M. B., & Shalimov, L. S. (2000). Lithosphere-ionosphere coupling and their modelling. *Russian J.*
685 *Terrestrial Sciences*, 2(2), 95–108.
- 686 Hao, J., Qian, S., Zhou, J., & Zhu, T. (2003). ULF electric and magnetic anomalies accompanying the cracking of
687 rock sample. *Acta Seismol. Sin.*, 25, 102–111 (in Chinese with English abstract).
- 688 Hayakawa, M., & Pulinets, S. (2010). Lithosphere-atmosphere-ionosphere coupling (laic) model. In
689 Electromagnetic Phenomena Associated with Earthquakes. *Transworld Research Network: Trivandrum, India.*
690 <https://doi.org/10.1016/j.jseaes.2010.03.005>
- 691 Hayakawa, M., Schekotov, A., Potirakis, S., Eftaxias, K., Li, Q., & Asano, T. (2015). An integrated study of ULF
692 magnetic field variations in association with the 2008 Sichuan earthquake, on the basis of statistical and critical
693 analyses. *Open J. Earthq. Res.*, 4, 85–93. <https://doi.org/10.4236/ojer.2015.43008>
- 694 He, Y., Yang, D., Qian, J., & Parrot, M. (2011). Response of the ionospheric electron density to different types of
695 seismic events. *Nat. Hazards Earth Syst. Sci.*, 11, 2173–2180. <https://doi.org/10.5194/nhess-11-2173-2011>
- 696 Heavlin, W. D., Kappler, K., Yang, L., Fan, M., Hickey, J., Lemon, J., MacLean, L., Bleier, T., Riley, P., &
697 Schneider, D. (2022). Case-control study on a decade of ground-based magnetometers in California reveals
698 modest signal 24–72 hr prior to earthquakes. *J. Geophys. Res. Solid Earth*, 127, e2022JB024109.
- 699 He, L., & Heki, K. (2016). Threedimensional distribution of ionospheric anomalies prior to three large earthquakes
700 in Chile. *Geophys. Res. Lett.*, 43, 7287–7293. <https://doi.org/10.1002/2016GL069863>
- 701 He, L., & Heki, K. (2018). Three-dimensional tomography of ionospheric anomalies immediately before the 2015
702 Illapel earthquake, Central Chile. *J. Geophys. Res. Space Physics*, 123. <https://doi.org/10.1029/2017JA024871>
- 703 Hough, S. (2020). The great quake debate: the crusader, the skeptic, and the rise of modern seismology. *Hough:*
704 *University of Washington Press.*
- 705 Hsiao, C. C., Liu, J. Y., Oyama, K. I., Yen, N. L., Liou, Y. A., Chen, S. S., & Miao, J. J. (2010).
706 Seismo-ionospheric precursor of the 2008 M_w 7.9 wenchuan earthquake observed by formosat-3/cosmic. *GPS*
707 *Solut.*, 14, 83–89. <https://doi.org/10.1007/s10291-009-0129-0>
- 708 Huang, Q. (2011). Rethinking earthquake-related DC-ULF electromagnetic phenomena: Towards a physics-based
709 approach. *Nat. Hazards Earth Syst. Sci.*, 11, 2941–2949. <https://doi.org/10.5194/nhess-11-2941-2011>
- 710 Huang, Q., & Lin, Y. (2010). Selectivity of seismic electric signal (SES) of the 2000 Izu earthquake swarm: a 3D
711 FEM numerical simulation model. *Proc. Jpn. Acad., Ser.*, 86(3), 257–264. <https://doi.org/10.2183/pjab.86.257>
- 712 Hu, J., Liu, W., Guo, M., & Zheng, H. (2009). The “double low-points” anomaly of daily vertical component
713 variation of geomagnetic field before the M 8.0 Wenchuan earthquake. *Acta Seismol. Sin.*, 31, 589–593.
714 (in Chinese with English abstract).
- 715 Jin, X., Zhang, L., Bu, J., Qiu, G., Ma, L., Liu, C., & Li, Y. (2020). Discussion on anomaly of atmospheric
716 electrostatic field in wenchuan M_s 8.0 earthquake. *Journal of Electrostatics*, 104(1).
- 717 Key, K. (2009). 1-D inversion of multicomponent, multi-frequency marine CSEM data: Methodology and
718 synthetic studies for resolving thin resistive layers. *Geophysics*, 74, 9–20, 2009.
719 <https://doi.org/10.1190/1.3058434>
- 720 Kim, V. P., & Hegai, V. V. (1999). A possible presage of strong earthquakes in the night-time mid-latitude F2
721 region ionosphere, in Atmospheric and Ionospheric Electromagnetic Phenomena Associated With Earthquakes,
722 pp. 619–627, *Terra Sci., Tokyo.*
- 723 Kuo, C. L., Huba, J. D., Joyce, G., & Lee, L. C. (2011). Ionosphere plasma bubbles and density variations induced
724 by pre-earthquake rock currents and associated surface charges. *J. Geophys. Res.*, 116, A10317.
725 <https://doi.org/10.1029/2011ja016628>
- 726 Kuo, C. L., Lee L. C., & Huba, J. D. (2014). An improved coupling model for the



- 727 lithosphere-atmosphere-ionosphere system. *J. Geophys. Res. Space Physics*, 119(4), 3189–3205.
728 <https://doi.org/10.1002/2013JA019392>
- 729 Li, M., Tan, H., Cao, M. (2016). Ionospheric influence on the seismo-telluric current related to electromagnetic
730 signals observed before the Wenchuan M_S 8.0 earthquake. *Solid Earth*, 7, 1405–1415.
731 <https://doi.org/10.5194/se-7-1405-2016>
- 732 Li, M. & Lu, J. (2009) ULF electromagnetic abnormality recorded at Gaobeidian and Ningjin stations before
733 Wenchuan 8.0 earthquake. *Int. Seismol. Dynam.*, 367, 76–82, 2009 (in Chinese with English abstract).
- 734 Li, M., Lu, J., Parrot, M., Tan, H., Chang, Y., Zhang, X., & Wang, Y. (2013). Review of unprecedented ULF
735 electromagnetic anomalous emissions possibly related to the Wenchuan $M_S = 8.0$ earthquake, on 12 May 2008.
736 *Nat. Hazards Earth Syst. Sci.*, 13(2), 279–286. <https://doi.org/10.5194/nhess-13-279-2013>
- 737 Li, M., Lu, J., Zhang, X., & Shen, X. (2019). Indications of Ground-based Electromagnetic Observations to A
738 Possible Lithosphere-Atmosphere-Ionosphere Electromagnetic Coupling before the 12 May 2008 Wenchuan M_S
739 8.0 Earthquake. *Atmosphere*, 10(7), 355. <https://doi.org/10.3390/atmos10070355>
- 740 Li, M., Jiang, X., Li, J., Zhang, Y., & Shen, X. (2023). Temporal-spatial characteristics of seismo-ionospheric
741 influence observed by the CSES satellite. *Advances in Space Research*.
742 <https://doi.org/10.1016/j.asr.2023.07.044>
- 743 Liperovsky, V. A., Pokhotelov, O. A., Meister, C.-V., & Liperovskaya, E.V. (2007). Physical models of coupling
744 in the lithosphere-atmosphere-ionosphere system before earthquakes. *Geomagnetism & Aeronomy*, 48 (48),
745 795–806. <https://doi.org/10.1134/S0016793208060133>
- 746 Li, Q., Schekotov, A., Asano, T., & Hayakawa, M. (2015). On the anomalies in ULF magnetic field variations
747 prior to the 2008 Sichuan earthquake. *Open J. Earthq. Res.*, 4, 55–64. <https://doi.org/10.4236/ojer.2015.42005>
- 748 Liu, J.Y., Chen, Y.I., Chen, C.H., Liu, C.Y., Chen, C.Y., Nishihashi, M., Li, J. Z., Xia, Y.Q., Oyama, K. I., Hattori,
749 K. (2009). Seismoionospheric GPS total electron content anomalies observed before the 12 May 2008 M_W 7.9
750 Wenchuan earthquake. *J. Geophys. Res.*, 114, A04320. <https://doi.org/10.1029/2008JA013698>
- 751 Liu, J. Y., Chen, Y. I., Huang, C. C., Parrot, M., Shen, X. H., Pulinet, S. A., Yang, Q. S., & Ho, Y.Y. (2015). A
752 spatial analysis on seismo-ionospheric anomalies observed by DEMETER during the 2008 M 8.0 Wenchuan
753 earthquake. *J. Asian Earth Sci.*, 114, S1367912015003399. <https://doi.org/10.1016/j.jseae.2015.06.012>
- 754 Ma, X., Lin, Z., Chen, H., Jin, H., Liu, X., & Jiao, L. (2014). Analysis on ionospheric perturbation of TEC and
755 NmF2 based on GPS and COSMIC data before and after the Wenchuan earthquake. *Chin. J. Geophys.*, 57,
756 2415–2422 (in Chinese with English abstract).
- 757 Maurya, A. K., Singh, R., Veenadhari, B., Kumar, S., & Singh, A. K. (2013). Sub-ionospheric very low frequency
758 perturbations associated with the 12 May 2008 $M = 7.9$ Wenchuan earthquake. *Nat. Hazards Earth Syst. Sci.*, 13,
759 2331–2336. <https://doi.org/10.5194/nhess-13-2331-2013>
- 760 Meister, C. V., Mayer, B., Dziendzie, P., Fulbert, F., Hoffmann, D. H. H., & Liperovsky, V. A. (2011). On the
761 acoustic model of lithosphere-atmosphere-ionosphere coupling before earthquakes. *Nat. Hazards Earth Syst.*
762 *Sci.*, 11(4), 1011–1017. <https://doi.org/10.5194/nhess-11-1011-2011>
- 763 Molchanov, O. A., Fedorov, E., Schekotov, A., Gordeev, E., Chebrov, V., Surkov, V., Rozhnoi, A., Andreevsky,
764 S., Iudin, D., Yunga, S., Lutikov, A., Hayakawa, M., & Biagi, P. F. (2004).
765 Lithosphere-atmosphere-ionosphere coupling as governing mechanism for preseismic short-term events in
766 atmosphere and ionosphere. *Nat. Hazards Earth Syst. Sci.*, 4 (5–6), 757–767.
767 <https://doi.org/10.5194/nhess-4-757-2004>
- 768 Namgaladze, A. A., Zolotov, O. V., Karpov, M. I., & Romanovskaya, Y. V. (2012). Manifestations of the
769 earthquake preparations in the ionosphere total electron content variations. *Natural Science*, 4(11), 848–855.
770 <https://doi.org/10.4236/ns.2012.411113>



- 771 Onishi, T., Berthelier, J. J., & Kamogawa, M. (2011). Critical analysis of the electrostatic turbulence
772 enhancements observed by DEMETER over the Sichuan region during the earthquake preparation. *Nat. Hazards*
773 *Earth Syst. Sci.*, *11*, 561–570. <https://doi.org/10.5194/nhess-11-561-2011>
- 774 Prescott, H. (2019). Pre-earthquake processes: a multidisciplinary approach to earthquake prediction
775 studies. *International Geology Review*, *61*(16), 2080–2082. <https://doi.org/10.1080/00206814.2019.1579001>
- 776 Pulinets, S. A., & Davidenko, D. (2014). Ionospheric precursors of earthquakes and Global Electric Circuit. *Adv.*
777 *Space Res.*, *53*(5): 709–723. <https://doi.org/10.1016/j.asr.2013.12.035>
- 778 Pulinets, S. A., & Boyarchuk, K. A. (2004). Ionospheric Precursors of Earthquakes. *Springer: Berlin/Heidelberg,*
779 *Germany.*
- 780 Pulinets, S. A., & Ouzounov, D. (2010). Lithosphere-Atmosphere-Ionosphere Coupling (LAIC) model-An unified
781 concept for earthquake precursors validation. *J. Southeast Asian Earth Sci.*, *41*(4–5), 371–382.
782 <https://doi.org/10.1016/j.jseaes.2010.03.005>
- 783 Pulinets, S. A., Boyarchuk, K. A., Hegai, V. V., Kim, V. P., & Lomonosov, A. M. (2000). Quasielectrostatic model
784 of atmosphere-thermosphere-ionosphere coupling. *Adv. Space Res.*, *26*(8): 1209–1218.
785 [https://doi.org/10.1016/S0273-1177\(99\)01223-5](https://doi.org/10.1016/S0273-1177(99)01223-5)
- 786 Pulinets, S. A., Boyarchuk, K. A., Hegai, V. V., Kim, V. P., & Lomonosov, A. M. (2000). Quasielectrostatic
787 model of atmosphere-thermosphere ionosphere coupling. *Adv. Space Res.*, *26*(8), 1209–1218.
788 [https://doi.org/10.1016/S0273-1177\(99\)01223-5](https://doi.org/10.1016/S0273-1177(99)01223-5)
- 789 Pulinets, S.A., Bondur, V.G., Tsidilina, M.N., & Gaponova, M.V. (2009). Verification of the concept of
790 seismoionospheric coupling under quiet heliogeomagnetic conditions, using the Wenchuan (China) earthquake
791 of 12 May 2008, as an example. *Geomagn. Aeron.*, *50*, 231–242. <https://doi.org/10.1134/S0016793210020118>
- 792 Qian, S., Hao, J., Zhou, J., & Gao, J. (2003). Precursory Electric and Magnetic Signals at ULF and LF Bands
793 during the Fracture of Rocks under Pressure. *Earthquake Research in China*, *19*, 109–116 (in Chinese with
794 English abstract).
- 795 Qian, S., Ren, K., & Lü Z. (1996). Experimental study on VLF, MF, HF and VHF electromagnetic radiation
796 characteristics with the rock breaking. *Earthquake Science*, *18*, 346–351 (in Chinese with English abstract).
- 797 Ren, H., Chen, X., & Huang, Q. (2012). Numerical simulation of coseismic electromagnetic fields associated with
798 seismic waves due to finite faulting in porous media. *Geophys. J. Int.*, *188*(3), 925–944.
799 <https://doi.org/10.1111/j.1365-246X.2011.05309.x>
- 800 Sorokin, V. M., & Hayakawa, M. (2013). Generation of Seismic-Related DC Electric Fields and
801 Lithosphere-Atmosphere-Ionosphere Coupling. *Mod. Appl. Sci.*, *7*(6), 1–25.
- 802 Richmond, A. D., Ridley, E. C., & Roble G. A. (1992). A thermosphere/ionosphere general circulation model with
803 coupled electrodynamics. *Geophys. Res. Lett.*, *19*(6), 601–604
- 804 Roble, R. G., Ridley, E. C., Richmond, A. D., & Dickinson, R. E. (1988). A coupled thermosphere general
805 circulation model. *Geophysical Research Letters*, *15*(12). <https://doi.org/10.1029/GL015i012p01325>
- 806 Rougier, J., Guillas, S., Maute, A., & Richmond, A. D. (2007). Emulating the Thermosphere-Ionosphere
807 Electrodynamics General Circulation Model (TIE-GCM). *Geoscientific model development*.
808 <https://doi.org/10.5194/gmd-2-59-2009>
- 809 Ruzhin, Y. Y., Sorokin, V. M., & Yashchenko, A. K. (2014). Physical Mechanism of Ionospheric Total Electron
810 Content Perturbations over a Seismoactive Region. *Geomagnetism and Aeronomy*, *54*(3), 337–346.
811 <https://doi.org/10.1134/S001679321403013X>
- 812 Ryu, K., Parrot, M., Kim, S. G., Jeong, K. S., Chae, J. S., Pulinets, S., & Oyama, K. I. (2014). Suspected
813 seismo-ionospheric coupling observed by satellite measurements and GPS TEC related to the M7.9 Wenchuan
814 earthquake of 12 May 2008. *J. Geophys. Res. Space Phys.*, *119*, 305–323. <https://doi.org/10.1071/ZO9930037>



- 815 <https://doi.org/10.5194/angeo-28-1615-2010>
- 816 Scoville, J., Sornette, J., & Freund, F. (2015). Paradox of peroxy defects and positive holes in rocks Part II:
817 Outflow of electric currents from stressed rocks. *J. Asian Earth Sci.*, *114*, 338–351.
818 <https://doi.org/10.1016/j.jseaes.2015.04.016>
- 819 Sorokin, V. M., & Hayakawa, M. (2014). Plasma and electromagnetic effects caused by the seismic-related
820 disturbances of electric current in the global circuit. *Mod. Appl. Sci.*, *8*(4), 61–83.
821 <https://doi.org/10.5539/mas.v8n4p61>
- 822 Sun, Y., Oyama, K.-I., Liu, J., Jhuang, H., & Cheng, C. (2011). The neutral temperature in the ionospheric dynamo
823 region and the ionospheric F region density during Wenchuan and Pingtung Doublet earthquakes.
824 *Nat. Hazards Earth Syst. Sci.*, *11*, 1759–1768. <https://doi.org/10.5194/nhess-11-1759-2011>
- 825 Walker, S. N., Kadirkamanathan, V., & Pokhotelov, O. A. (2013). Changes in the ultra-low frequency wave field
826 during the precursor phase to the Sichuan earthquake: DEMETER observations. *Ann. Geophys.*, *31*, 1597–1603.
827 <https://doi.org/10.5194/angeo-31-1597-2013>
- 828 Wang, W., Ding, J., Yu, S., & Zhang, Y. (2009). Short-term geomagnetic abnormality before Wenchuan M_s 8.0
829 earthquake and strong earthquake prediction explore. *Earthq. Sci.*, *31*, 172–179 (in Chinese with English
830 abstract).
- 831 Yan, X., Shan, X., Cao, J., Tang, J., & Wang, F. (2012). Seismoionospheric anomalies observed before the
832 Wenchuan earthquake using GPS and DEMETER data. *Seismol. Geol.*, *34*, 160–171 (in Chinese with English
833 abstract). <https://doi.org/10.3969/j.issn.0253-4967.2012.01.015>
- 834 Yang, X., Zhou, C., Liu, J., Zhao, Y., & Zhang, Y. (2014). A numerical study of seismic-related electric field in
835 the ionosphere. *Chinese J. Geophys.*, *57*(11), 3650–3658. <https://doi.org/10.6038/cjg20141119>
- 836 Yu, T., Mao, T., Wang, Y., & Wang, J. (2009). Study of the ionospheric anomaly before the Wenchuan earthquake.
837 *Chin. Sci. Bull.*, *54*, 1086–1092 (in Chinese with English abstract).
- 838 Zeng, Z., Zhang, B., Fang, G., Wang, D., & Yin, H. (2009). The analysis of ionospheric variations before the
839 Wenchuan earthquake with DEMETER data. *Chinese J. Geophys.*, *52*, 11–19 (in Chinese with English abstract).
- 840 Zhang, Y., Feng, W., Xu, L., Zhou, C., & Chen, Y. (2009a). Spatio-temporal rupture process of the 2008 great
841 Wenchuan earthquake. *Science China Ser. D*, *52*, 145–154.
- 842 Zhang, X., Ding, J., Shen, X., Wang, M., & Ouyang, X. (2009b). Electromagnetic perturbations before wenchuan
843 M₈ earthquake and stereo electromagnetic observation system. *Chinese Journal of Radio Science*, *24*(1), 1–8.
844 [https://doi.org/10.1016/S1874-8651\(10\)60080-4](https://doi.org/10.1016/S1874-8651(10)60080-4)
- 845 Zhao, B., Yu, T., Wang, M., Wan, W., Lei, J., Liu, L., & Ning, B. (2008). Is an unusual large enhancement of
846 ionospheric electron density linked with the 2008 great Wenchuan earthquake? *J. Geophys. Res.*, *113*, A11304.
- 847 Zhao, B., Wang, M., Yu, T., Xu, G., Wan, W., & Liu, L. (2010). Ionospheric total electron content variations prior
848 to the 2008 Wenchuan Earthquake. *Int. J. Remote Sens.*, *31*, 3545–3557.
849 <https://doi.org/10.1080/01431161003727622>
- 850 Zolotov, O. V., Namgaladze, A. A., Zakharenkova, I. E., Martynenko, O. V., & Shagimuratov, I. I. (2012).
851 Physical Interpretation and Mathematical Simulation of Ionospheric Precursors of Earthquakes at Midlatitudes.
852 *Geomagnetism & Aeronomy*, *52*(3), 390–397. <https://doi.org/10.1134/s0016793212030152>
- 853 Zolotov, O. V. (2015). Ionosphere Quasistatic Electric Fields Disturbances over Seismically Active Regions as
854 Inferred from Satellite-Based Observations: A Review. *Russian Journal of Physical Chemistry B*, *9*(5), 785–
855 788.
- 856 Zhou, C., Liu, Y., Zhao, S., Liu, J., Zhang, X., & Huang, J., Shen, X., Ni, B., & Zhao, Z. (2017). An electric field
857 penetration model for seismo-ionospheric research. *Adv. Space Res.*, 2217–2232.
858 <https://doi.org/10.1016/j.asr.2017.08.007>



859 Zhu, F., Wu, Y., Lin, J., Zhou, Y., Xiong, J., & Yang, J. (2009). Anomalous response of ionospheric VTEC before
860 the Wenchuan earthquake. *Acta Seismol. Sin.*, 31, 180–187. [https://doi.org/10.1016/S1874-8651\(10\)60080-4](https://doi.org/10.1016/S1874-8651(10)60080-4)
861